Environmental Science and Ecotechnology 29 (2026) 100663

Contents lists available at ScienceDirect

Environmental Science and Ecotechnology

journal homepage: www.journals.elsevier.com/environmental-science-and-ecotechnology/

Original Research

Weighted network analysis of adverse outcome pathways decodes the multiscale mechanisms of environmental toxicity

Huajie Yang [a,b,c,1], Kaiyi Zhang [d,1], Yue Wang [e], Shuailing Liu [f], Yinchu Guo [g], Wei Liu [h], Jiaxing Sun [i], Zhaoqi Zhang [j], Sen Zhang [j], Shenghang Li [k], Yingcheng Zhao [l], Tong Liu [m], Junhong Liu [n], Liang Pei [o], Shuhua Xi [j,o], Peng Shi [g,o,*]

[a] Department of Occupational and Environmental Health, School of Public Health, Tianjin Medical University, Tianjin, 300070, PR China
[b] Tianjin Key Laboratory of Environment Nutrition and Public Health and Key Laboratory of Prevention and Control of Major Diseases in the Population, Ministry of Education, Tianjin Medical University, Tianjin, 300070, PR China
[c] Center for International Collaborative Research on Environment Nutrition and Public Health, Tianjin, 300070, PR China
[d] Department of Accounting, The First Affiliated Hospital of China Medical University, Shenyang, 110001, PR China
[e] Department of Epidemiology, School of Public Health, Shenyang Medical College, Shenyang, 110034, PR China
[f] College of Health Management, China Medical University, No. 77 Puhe Road, Shenyang North New Area, Shenyang, 110122, Liaoning, PR China
[g] Department of Epidemiology, School of Public Health, China Medical University, Shenyang, 110122, PR China
[h] Department of Biomedical-Engineering, School of Intelligent Medicine, China Medical University, Shenyang, 110122, PR China
[i] Department of Ultrasound, Shengjing Hospital of China Medical University, Shenyang, 110004, PR China
[j] Department of Environmental Health, School of Public Health, China Medical University, Shenyang, 110122, PR China
[k] Department of Nutrition and Food Hygiene, School of Public Health, China Medical University, Shenyang, 110122, PR China
[l] The First Clinical College, China Medical University, Shenyang, 110122, PR China
[m] School of Clinical Medical, China Medical University, Shenyang, 110122, PR China
[n] Preventive Medicine, School of Public Health, China Medical University, Shenyang, 110122, PR China
[o] Key Laboratory of Environmental Stress and Chronic Disease Control and Prevention, Ministry of Education, China Medical University, Shenyang, 110122, PR China

ARTICLE INFO

Article history:
Received 21 July 2025
Received in revised form
21 January 2026
Accepted 23 January 2026

Keywords:
Environmental toxicology
Adverse outcome pathways
Phenotype-disease mapping
Chemical-disease mechanisms
Predictive toxicology

ABSTRACT

The rapid proliferation of synthetic chemicals has significantly outpaced traditional toxicity characterization, leaving a critical data gap in environmental health risk assessment. While the adverse outcome pathway (AOP) framework provides a mechanistic scaffold for organizing toxicity knowledge, it is currently limited by a focus on linear pathways and a bias toward well-studied endpoints. Conversely, the exposome paradigm captures broad environmental stressors but often lacks the mechanistic depth required for causal interpretation. A fundamental challenge remains in developing integrative paradigms that can systematically bridge these multi-scale datasets to decode complex, chemical-induced diseases. Here we show that AOP-ExpoVis, an integrative computational platform, synergizes exposome-disease networks with AOP ontologies to prioritize pathogenic mechanisms through a weighted phenotype-disease scoring algorithm. By integrating chemical, gene, phenotype, and disease associations, the platform identifies key phenotypes and maps them to curated pathways to generate testable mechanistic hypotheses. Validation across three distinct case studies involving 2,2′,4,4′-tetrabromodiphenyl ether (BDE-47), arsenic, and perfluoroalkyl substances (PFAS) demonstrated that AOP-ExpoVis accurately identifies both conserved and chemical-specific toxic pathways, such as aryl hydrocarbon receptor activation and lipid metabolism disruption. AOP-ExpoVis provides an open-source tool for rapid mechanistic inference that overcomes the limitations of traditional, single-pathway frameworks. This work advances predictive toxicology by enabling the systematic prioritization of chemical hazards and the refinement of regulatory risk assessment in a data-rich environment.

* Corresponding author. Key Laboratory of Environmental Stress and Chronic Disease Control and Prevention, Ministry of Education, China Medical University, Shenyang, 110122, PR China.
E-mail address: pshi@cmu.edu.cn (P. Shi).
[1] Contribute equally to this work.

https://doi.org/10.1016/j.ese.2026.100663

1. Introduction

Modern environmental toxicology faces a data crisis. Tens of thousands of synthetic chemicals are used despite minimal characterization of their toxicity. Over 350,000 chemicals are on the market globally, and traditional one-at-a-time testing cannot feasibly keep pace [1]. Most of these substances remain "data-poor," with clear information on their mechanisms of action or health effects notably lacking [2]. This gap undermines risk assessment and public health, especially when real-world exposures involve dynamic mixtures interacting with biological networks in non-additive ways [3]. New frameworks capable of rapidly elucidating toxicological mechanisms across multiple stressors are urgently needed. Therefore, to address this data crisis, the key lies in developing a new paradigm that can both efficiently integrate existing data and systematically characterize toxicological mechanisms. This is precisely the problem that the adverse outcome pathway (AOP) framework seeks to solve.

AOP provides a mechanistic scaffold for organizing knowledge of toxicity. An AOP is a formalized sequence of key biological events that links a molecular initiating event to an adverse outcome at the organism level [4,5]. By delineating these cause-and-effect chains, AOPs impart mechanistic specificity to in vitro and in vivo findings and aid extrapolation across biological levels and species. However, the current catalog of AOPs is limited and biased toward well-studied endpoints. Only a few hundred AOPs have been established (with many still under development) [6], leaving most toxic effects without defined pathways. This incomplete coverage reflects a knowledge bias: Toxicology efforts gravitate toward known mechanisms and may overlook novel or complex pathways [7]. Furthermore, individual AOPs are typically linear and single-outcome, whereas real-world toxicants often trigger multiple interlinked pathways in parallel [8].

A complement to the depth of AOPs is the exposome paradigm, which broadens the scope of toxicology to consider the exposome—the totality of environmental exposures an organism encounters over its life course [9]. Exposomics employs high-throughput, untargeted analyses to profile many chemicals and stressors in parallel, thereby inherently accounting for mixtures and co-exposures [10]. This broad view is invaluable for discovering exposure–disease associations at a systems level. However, exposomic studies often yield correlations without offering clear mechanistic interpretations. Mechanistic toxicology frameworks, such as AOP, are needed to translate exposomic signals into causal explanations [11]. In other words, exposomics can reveal which exposures correlate with adverse outcomes, while an AOP lens explains how those exposures lead to harm. This complementarity calls for an integrated computational approach that combines exposome-wide data with pathway-level insight.

In this study, we propose a novel systems-based framework inspired by network theory and weighted gene co-expression network analysis (WGCNA) [12]. This framework facilitates the identification of pivotal phenotypes linking chemical exposures to adverse outcomes. Key to this approach is the concept of centrality, a network metric that quantifies the importance of phenotypes within a dynamic exposure–disease network. In this framework, central phenotypes act as key hubs that link environmental factors to adverse health effects. Comprehensive toxicological databases, such as the Comparative Toxicogenomics Database (CTD) [13], along with recent advances in multi-omics technologies, have created unprecedented opportunities to integrate vast amounts of heterogeneous data.

However, traditional frameworks often fail to account for the context-dependent nature of toxicity. The same chemical exposure may perturb multiple biological pathways, with effects that diverge or converge, depending on the biological system in question. To overcome this limitation, we introduce AOP-ExpoVis, a computational platform that redefines toxicity pathway discovery by integrating exposome–disease networks with AOP ontologies. The platform's core algorithm employs a weighted phenotype–disease (WPD) scoring system to quantitatively prioritize phenotypes based on their topological centrality within the exposure–disease network and their semantic alignment with established AOP key events (KEs). Through iterative phenotype weighting informed by WPD scores and semi-supervised learning, AOP-ExpoVis enables the dynamic identification of KEs and their interdependencies, thus offering a more accurate and contextually relevant understanding of chemical toxicity. This approach enhances the predictive power of existing toxicological models and provides a novel framework for mapping the intricate, multidimensional interactions between health outcomes and environmental pollutants.

To demonstrate the versatility and experimental robustness of this approach, we apply AOP-ExpoVis to three well-characterized environmental contaminants with established toxicological associations but incompletely understood mechanisms:

i. 2,2′,4,4′-tetrabromodiphenyl ether (BDE-47) [14], recognized for its neurotoxicity;
ii. Arsenic, a Class I human carcinogen linked to increased breast cancer risk [15]; and
iii. Perfluorooctanoic acid (PFOA) and perfluorooctane sulfonic acid (PFOS) [16], which have been associated with liver dysfunction and fatty liver disease.

For each of these chemicals, we systematically construct toxicity pathway maps as follows:

1. For BDE-47, we combine AOP-ExpoVis-based predictions with in vitro transcriptomic validation to identify KEs leading to neurocognitive deficits;
2. For arsenic, we employ phenotypic intersection analysis and AOP enrichment screening to uncover potential toxic pathways linking exposure to breast cancer; and
3. For PFOA and PFOS, we use transcriptomic data from treated human hepatocellular carcinoma cells (HepG2) in the Gene Expression Omnibus (GEO) database to compare shared and chemical-specific mechanisms of liver injury.

Through these investigations, we aim to establish a comprehensive mechanistic framework that links chemical exposures to adverse health risks, providing a powerful tool to advance environmental health science and improve regulatory decision-making.

2. Materials and methods

2.1. Development of the AOP-ExpoVis platform

The AOP-ExpoVis platform was engineered as a comprehensive, web-based analytical environment using R v3.6.1 and the Shiny framework. This platform integrates chemical–phenotype–disease associations with AOPs to facilitate the exploration of toxicological mechanisms. Central to this integration is the WPD scoring system, which quantifies the strength of associations between chemicals and disease endpoints by integrating multi-source evidence. This score allows for the ranking and prioritization of potential toxicological links. For the comprehensive algorithms, detailed processes, and specific parameter settings used in the development

and implementation of the AOP-ExpoVis platform, please refer to Supplementary Method.

2.1.1. Data acquisition and preparation

Datasets encompassing chemical–phenotype–disease associations were sourced from the CTD (http://ctdbase.org/), ensuring extensive coverage of relevant associations [13]. Phenotypes were systematically mapped to their corresponding Gene Ontology (GO) terms, while diseases were categorized based on the Medical Subject Headings (MeSH) hierarchy. Data harmonization was conducted to standardize chemical names by consolidating multiple aliases and identifiers into a consistent nomenclature. Filtering procedures were applied to exclude records with non-specific phenotypes or incomplete mappings, thereby enhancing the quality and reliability of the data. Subsequently, datasets were merged by using common identifiers, such as gene symbols, chemical names, and disease IDs, to construct a unified network encompassing genes, chemicals, phenotypes, and diseases. AOP data and KE information were obtained from the AOP-Wiki database (https://aopwiki.org/) as structured datasets containing KE definitions, relationships, and biological components. Detailed information is provided (Supplementary Method Sections 1.1 and 1.2).

2.1.2. Network architecture and the WPD scoring algorithm

The curated associations were formalized as a heterogeneous, undirected graph $\Gamma = (\boldsymbol{V}, \boldsymbol{E}, w)$. The vertex set $\boldsymbol{V}$ comprises chemicals (C), genes (G), phenotypes (PH), and diseases (D), and the edge set $\boldsymbol{E}$ represents binary associations between these entities (e.g., C–G, G–PH). We defined an evidence-weighted adjacency matrix $\boldsymbol{A}$, with edge weights (w_{ij}) calculated using equation (1):

$$w_{ij} = \frac{N_{ij}}{\sum_k N_{ik}} \tag{1}$$

where N_{ij} is the number of peer-reviewed articles in CTD supporting the specific association between entities i and j, and $\sum_k N_{ik}$ represents the total number of studies supporting all associations involving entity i. This normalization mitigates bias from highly studied entities. Nodes represent entities, while edges encode weighted interactions. Degree centrality for genes and chemicals is computed by summing weighted connections to phenotypes and diseases and then quantifying node importance based on connectivity.

The statistical significance of overlaps between distinct entity sets (e.g., phenotypes associated with specific chemicals and diseases) was evaluated using a hypergeometric test. We computed the probability of observing (equation (2)) at least m shared entities under random sampling without replacement:

$$P(X \geq m) = \sum_{k=m}^{\min(n_x, n_y)} \frac{\binom{A}{B}\binom{N-k}{n_x-k}\binom{N-n_x}{n_y-k}}{\binom{N}{n_x}\binom{N}{n_y}} \tag{2}$$

where $\binom{A}{B}$ denotes the binomial coefficient, which represents the number of ways that B elements can be chosen from a set of A elements, N represents the total number of entities (genes or chemicals), m is the number of overlapping entities observed, and n_x and n_y are the sizes of the two individual sets being compared. This calculation helps determine whether the observed overlap exceeds what would be expected by chance.

The WPD score is a composite metric designed to quantify the relevance of KEs within the integrated exposome–AOP network by synergistically combining two computational approaches: hypergeometric scoring and degree centrality. For each KE, the WPD_i score is defined as:

$$\begin{aligned} WPD_i = -\Big[& W_{\text{gene}} \times \left(\log_{10} p_{\text{gene}} + \log_{10} p_{\text{gene,comb}}\right) \\ & + W_{\text{chemical}} \times \left(\log_{10} p_{\text{chemical}} + \log_{10} p_{\text{chemical,comb}}\right)\Big] \end{aligned} \tag{3}$$

where p_{gene} and p_{chemical} represent hypergeometric probabilities indicating the significance of gene and chemical associations, respectively; W_{gene} and W_{chemical} denote weight factors derived from degree centrality, reflecting the topological importance of genes and chemicals within the network; and $p_{\text{gene,comb}}$ and $p_{\text{chemical,comb}}$ correspond to combined hypergeometric probabilities that account for multi-entity associations. The detailed methodologies underlying the network construction process and WPD calculations are provided in Supplementary Method Sections 1.3 and 1.4.

2.1.3. Integration with adverse outcome pathways

To bridge computationally derived phenotype associations with established toxicological mechanisms, we systematically mapped all identified phenotypes to KEs within AOPs sourced from the AOP-Wiki database. This curated repository provides standardized descriptions and hierarchical relationships among molecular initiating events (MIEs), KEs, and adverse outcomes (AOs) (https://aopwiki.org/). For each phenotype, we matched its GO terms to the GO annotations associated with candidate KEs, and quantified the phenotype–KE association strength ($S_{\text{phenotype-KE}}$) as

$$S_{\text{phenotype-KE}} = \sum_{G_i \in G} W_{\text{gene}}(G_i) + \sum_{C_i \in C} W_{\text{chemical}}(C_i) \tag{4}$$

where G and C denote the sets of genes and chemicals associated with the phenotype, and $W_{\text{gene}}(G_i)$ and $W_{\text{chemical}}(C_i)$ are the corresponding entity weights. The detailed methodology is described in Supplementary Method Section 1.4.

2.1.4. Core algorithms

We assessed whether the phenotype data exhibited intrinsic clustering structure using the Hopkins statistic (H), computed with the factoextra R package, before performing cluster analysis. The statistic was defined as

$$H = \frac{\sum_{i=1}^{n} u_i}{\sum_{i=1}^{n} u_i + \sum_{i=1}^{n} w_i} \tag{5}$$

where u_i denotes the distance from a uniformly distributed random point to its nearest neighbor in the actual data, and w_i represents the distance from an actual data point to its nearest neighbor within the same dataset. A Hopkins statistic value close to 1, well above the 0.5 benchmark for randomness, indicates a strong clustering tendency, supporting the use of subsequent cluster-based analyses.

To evaluate the functional coherence of clustered phenotypes, the semantic similarity between GO terms was quantified using the R packages GOSemSim and GOSim with the Wang method [17–19]. This method measures the functional similarity between two GO terms by considering their locations in the GO graph structure as well as the semantic contributions of their ancestor terms. The resulting similarity score ranges from 0 to 1, reflecting the degree of functional relatedness between the terms based on the ontology's structure. High semantic similarity scores

(approaching 1) indicate that phenotypes within a cluster participate in overlapping biological processes, molecular functions, or cellular components, thereby validating the biological relevance and non-random nature of the identified clusters.

To enable consistent comparison of association strengths across phenotypes and chemicals, we converted phenotype-specific association strengths to rank percentiles. For each chemical, phenotypes were ranked by association strength, and the rank percentile for phenotype *i* was computed as its rank divided by the total number of phenotypes. Full algorithmic details, including formulas and implementation, are provided in Supplementary Method Section 1.5.

2.1.5. Implementation and visualization

The AOP-ExpoVis platform is a freely accessible, open-source tool with an intuitive user interface that enables seamless interaction and robust data exploration. It allows users to select chemicals and disease classifications, visualize complex chemical–phenotype–disease associations, perform detailed phenotype analyses, and interact with dynamic heatmaps that illustrate phenotype clustering across diverse disease endpoints. Implementation specifics and advanced visualization techniques are detailed in Supplementary Method Section 1.6, while Supplementary Method Section 1.7 provides comprehensive benchmarks of computational performance, highlighting the platform's scalability, runtime efficiency, and memory usage across datasets of varying sizes. For complete usage guidelines, including step-by-step instructions and examples, please refer to the user manual (Supplementary Text). The platform is accessible directly in a web browser, without additional software installation, at http://47.92.117.247:3838/AOP-ExpoVis. The source code is hosted on GitHub at https://github.com/HealthEWS/AOP-ExpoVis.

2.2. Case studies

To validate the practical utility of the AOP-ExpoVis framework, case studies were performed on three representative environmental contaminants with different health implications: BDE-47 (neurotoxicity), arsenic (breast cancer), and the perfluoroalkyl substances PFOA and PFOS (liver injury).

2.2.1. Data acquisition and phenotype association analysis

For the three target chemicals or chemical groups—BDE-47 (MeSH: C108444), arsenic (MeSH: D001151), and perfluoroalkyl substances (PFOA [MeSH: C023036] and PFOS [MeSH: C072883])—phenotypes demonstrating significant associations were retrieved from the CTD using their respective MeSH identifiers. Disease-related phenotypes were similarly obtained for each health outcome: cognitive dysfunction (including Alzheimer's disease [MeSH: D000544], Parkinson's disease [D010300], memory disorders [D008569], learning disabilities [D007859], and intellectual disability [D008607]), breast cancer (including breast neoplasms [D001943], inflammatory breast neoplasms [D058922], triple-negative breast neoplasms [D064726], and carcinoma, ductal, breast [D018270]), and liver diseases (including liver diseases [D008107], liver cirrhosis [D008103], hepatitis [D006505], fatty liver [D005234], and non-alcoholic fatty liver disease [D065626]). To systematically retrieve relevant KEs for each chemical, an AOP knowledge base-driven strategy was employed.

2.2.2. Identification and prioritization of shared phenotypes; AOP matching

To pinpoint core phenotypes implicated in chemical–disease associations, phenotypes shared by each chemical and their corresponding disease outcomes were first identified and considered as candidate KEs. A network topology-based algorithm was subsequently applied to compute the WPD score for each shared phenotype. The phenotypes were ranked by WPD scores, and high-ranking candidates were selected for cluster analysis to preliminarily elucidate potential mechanisms underlying contaminant-induced phenotypes. The optimal subset of phenotypes was determined using the Hopkins statistic, with a threshold of 0.5 or higher indicating a valid clustering structure. These phenotypes were then mapped to known KEs within the AOP-Wiki database to facilitate functional annotation and AOP inference. Final AOP screening was conducted based on enrichment ratios and quantitative scores. To enhance the biological relevance and accuracy of this screening, a functional-relevance filtering module embedded in the AOP-ExpoVis platform was employed. This module leveraged disease-specific keywords to refine the AOP selection: for BDE-47, terms such as “neuro” and “memory” were used; for arsenic, “cancer,” “breast,” and “fatty” were applied; and for the PFAS compounds, “liver” served as the primary filter.

2.2.3. In vitro validation of BDE-47-induced HT22 cell dysfunction

Cell culture and treatment. We cultured HT22 mouse hippocampal neuronal cells (purchased from Wuhan Pnosi Biological Technology Co., Ltd., Wuhan, China) in Dulbecco's Modified Eagle's Medium (DMEM, Gibco, New York, USA) supplemented with 10% fetal bovine serum (FBS, Biological Industries, Kibbutz Beit-Haemek, Israel), 100 U mL^{-1} penicillin, and 100 μg mL^{-1} streptomycin (Biological Industries, Kibbutz Beit-Haemek, Israel) under standard conditions (37 °C, 5% CO_2). The medium was refreshed every 48 h, and cells were subcultured at 80–90% confluence using 0.25% trypsin (Gibco, New York, USA). The cells were passaged at a 1:4 ratio and maintained at an appropriate density for subsequent experiments. To assess the toxicity of BDE-47 (CAS 5436-43-1, Beijing Huawei Ruike Chemical Co., Ltd., Beijing, China), cells were exposed to 2.5, 5, and 10 μM, representing low, medium, and high exposure levels, respectively. To evaluate aryl hydrocarbon receptor (AhR) involvement, the specific AhR antagonist CH-223191 (Cat. #C8124, CAS 301326-22-7, Sigma-Aldrich, St. Louis, MO, USA) was co-administered with BDE-47. Dimethyl sulfoxide (DMSO; final concentration 0.1%) served as the vehicle control. The experimental design comprised two parts: (1) dose-dependent cytotoxicity assessment of BDE-47 and (2) evaluation of AhR pathway involvement in BDE-47-induced responses.

Cell viability and morphological analysis. Cell viability was quantified using a Cell Counting Kit-8 (CCK-8; Cat. #C0038, Biyuntian Biotech, Shanghai, China), a colorimetric assay that measures WST-8 reduction to formazan by cellular dehydrogenases, following the manufacturer's instructions and established methodology [20]. Briefly, HT22 cells were seeded in 96-well plates (5000 cells $well^{-1}$), allowed to adhere overnight, and treated with BDE-47 for 24 h. Subsequently, 10 μL of CCK-8 solution was added per well, followed by incubation for 1 h at 37 °C in the dark. Absorbance was measured at 450 nm using a microplate reader (Model 1680, Bio-Rad Laboratories, California, USA), and viability was normalized to the control group. Morphological changes were observed under an inverted microscope (Olympus AX71 + 12FL/PH), and alterations in cell shape, adhesion, and density were evaluated. Images were captured from three independent wells per group, with at least three random fields per well.

Transcriptomic analysis and RT-qPCR validation. We extracted total RNA from HT22 cells exposed to 0, 2.5, 5, or 10 μM BDE-47 for 24 h using RNAiso Plus (Takara Biomedical Technology, Beijing, China). The quality of the RNA was assessed (NanoDrop for purity; Agilent 2100 Bioanalyzer for integrity; RNA integrity number [RIN] > 7). Ribosomal RNA was depleted, and strand-specific

complementary DNA (cDNA) libraries were prepared using the TruSeq Stranded mRNA Library Prep Kit (Illumina, USA). Paired-end sequencing (2 × 150 bp) was performed on an Illumina Novaseq 4000 platform (Suzhou GENEWIZ, Jiangsu, China). Raw reads were processed with fastp for quality control, and differential expression analysis was conducted using DESeq2. Functional enrichment of differentially expressed genes (DEGs) was analyzed via GO term enrichment (GOSeq package; $P \leq 0.05$) and Kyoto Encyclopedia of Genes and Genomes (KEGG) pathway analysis. Based on transcriptomic results, we selected two xenobiotic metabolism-related genes (*Gstp2* and *Ugt2b34*) for reverse transcription quantitative polymerase chain reaction (RT-qPCR) validation. cDNA was synthesized using the PrimeScript™ RT Reagent Kit (Takara Biomedical Technology, Beijing, China), and amplification was performed on a 7500 RTqPCR system (Applied Biosystems, Massachusetts, USA) using SYBR® Premix Ex Taq™ (Takara Biomedical Technology, Beijing, China). The primer sequences are listed (Supplementary Table S1). Relative expression was calculated using the $2^{-\Delta\Delta CT}$ method, with β-actin as the endogenous control.

Statistical analysis. Data are presented in the form of mean ± standard deviation (SD). We compared groups using one-way analysis of variance (ANOVA) with least significant difference (LSD) post hoc tests using SPSS 26.0 (IBM Corp, USA) and GraphPad Prism 8.0 (GraphPad Software, USA). Statistical significance was defined as $P < 0.05$.

2.2.4. Transcriptomic data analysis of PFOA and PFOS in HepG2 cells

Transcriptomic data for PFOA and PFOS were retrieved from the GEO database (accession: GSE266866), which profiles whole-genome expression in HepG2 following 24-h exposure to 35 μM of each compound. Raw expression matrices and the corresponding metadata were downloaded using the R package GEOquery. Data preprocessing, normalization, and differential expression analysis were performed using the limma package. DEGs were identified with a significance threshold of $P < 0.05$ and an absolute $\log_2$ fold change exceeding the mean ± 2 SD of the global expression variation. This approach—which is analogous to selecting outliers beyond the 95% confidence interval under a normal distribution—ensures that only the most robust and biologically relevant changes are considered. The DEGs were functionally annotated via GO and KEGG pathway enrichment analyses using the clusterProfiler package. Semantic similarity between GO terms was computed using the Wang method [21], which accounts for the topological structure of the GO directed acyclic graph. Hypergeometric testing with Benjamini–Hochberg correction for multiple comparisons was applied in both the GO and KEGG analyses to identify significantly altered biological processes and pathways.

2.2.5. Integration of computationally predicted phenotypes with transcriptomic enrichment profiles

To assess the concordance between computationally inferred KEs and empirical transcriptomic responses, we performed a systematic alignment based on the semantic similarity between GO terms. Phenotypes identified as potential KEs for chemical-induced diseases constituted the prediction set, while significantly enriched GO terms derived from RNA-seq data formed the experimental set. Pairwise semantic similarities between terms in both sets were calculated using the GOSemSim package with the Wang method. A predicted phenotype was considered validated if it exhibited high functional similarity (i.e., a semantic similarity score >0.7) with any term within the experimental enrichment set, indicating pathway-level consistency between the in silico predictions and the transcriptomic evidence [18].

3. Results and discussion

3.1. System overview and comparative advantage

We encoded disease–gene, chemical–disease, disease–phenotype, and chemical–phenotype associations in an adjacency matrix (Fig. 1a). Adopting the methodology established by King et al., we derived edge weights from manually curated evidence within the CTD [22]. To evaluate the statistical significance of shared phenotypes across chemicals and diseases, we used a hypergeometric test [23]. The model incorporated direct connectivity probabilities (p_{gene}, p_{chemical}) and combination probabilities ($p_{\text{gene,comb}}$, $p_{\text{chemical,comb}}$) to minimize bias from high-degree nodes (extensively studied chemicals or diseases), consistent with network-based ranking studies [24–26].

The WPD score (Fig. 1b) integrates gene- and chemical-derived hypergeometric probabilities into a unified metric, demonstrating conceptual alignment with the S_{XYA}/W_{XYA} framework [22]. This score prioritizes phenotypes associated with specific, low-connectivity genes or chemicals rather than hub-connected entities. We then clustered phenotypes based on the semantic similarity of their GO terms (Fig. 1c), forming toxicity modules supported by high Hopkins statistics (non-random clustering) and GOSemSim validation (biological coherence) [27]. These modules were mapped to known KEs in AOP-Wiki (Fig. 1d), thereby bridging predictions with established toxicity pathways.

AOP-ExpoVis diverges fundamentally from WGCNA (Supplementary Table S2)—which identifies co-expression modules based on transcriptomic data [12,28]—by integrating multi-scale evidence (chemicals, genes, phenotypes, and diseases) into a unified network using combinatorial mathematics and adjacency matrix operations. Whereas WGCNA outputs gene modules, AOP-ExpoVis generates WPD scores and phenotype clusters directly mappable to AOP KEs. This approach aligns with evidence that local network topology scoring outperforms correlation-based methods in ranking chemical–disease relationships [29]. Critically, AOP-ExpoVis prioritizes phenotypes mechanistically linked to chemical–disease pairs via low-degree associations, reducing obscuration by hub entities prevalent in large-scale databases. This established network analytical framework was subsequently applied to the three case studies to address their distinct mechanistic gaps: predicting neurotoxic pathways for BDE-47, uncovering breast cancer links for arsenic, and delineating shared vs. specific hepatotoxic mechanisms for PFOA and PFOS.

3.2. Platform implementation and workflow

AOP-ExpoVis was used to synthesize ten CTD-derived tables (including phenotype, chemical–disease, gene–phenotype, and hsGO) into a cohesive network. The phenotype table (>367,000 entries) linked chemicals to biological processes, while bp_phenotype_disease (>2.5 million records) connected GO terms to diseases. Chemical–disease associations (>8.6 million entries) integrated both curated and inferred evidence, with chemical_disease_curated (>100,000 records) providing high-confidence anchors. Disease hierarchies and gene–phenotype associations added ontological depth and mechanistic validation.

The platform employed local topology-aware scoring to mitigate hub bias. Macro-level visualizations highlighted high-frequency relationships (Fig. 2a–e), while users could inspect individual chemicals or diseases to access finer-grained information about related genes, phenotypes, and supporting evidence (Fig. 2f and Supplementary Text).

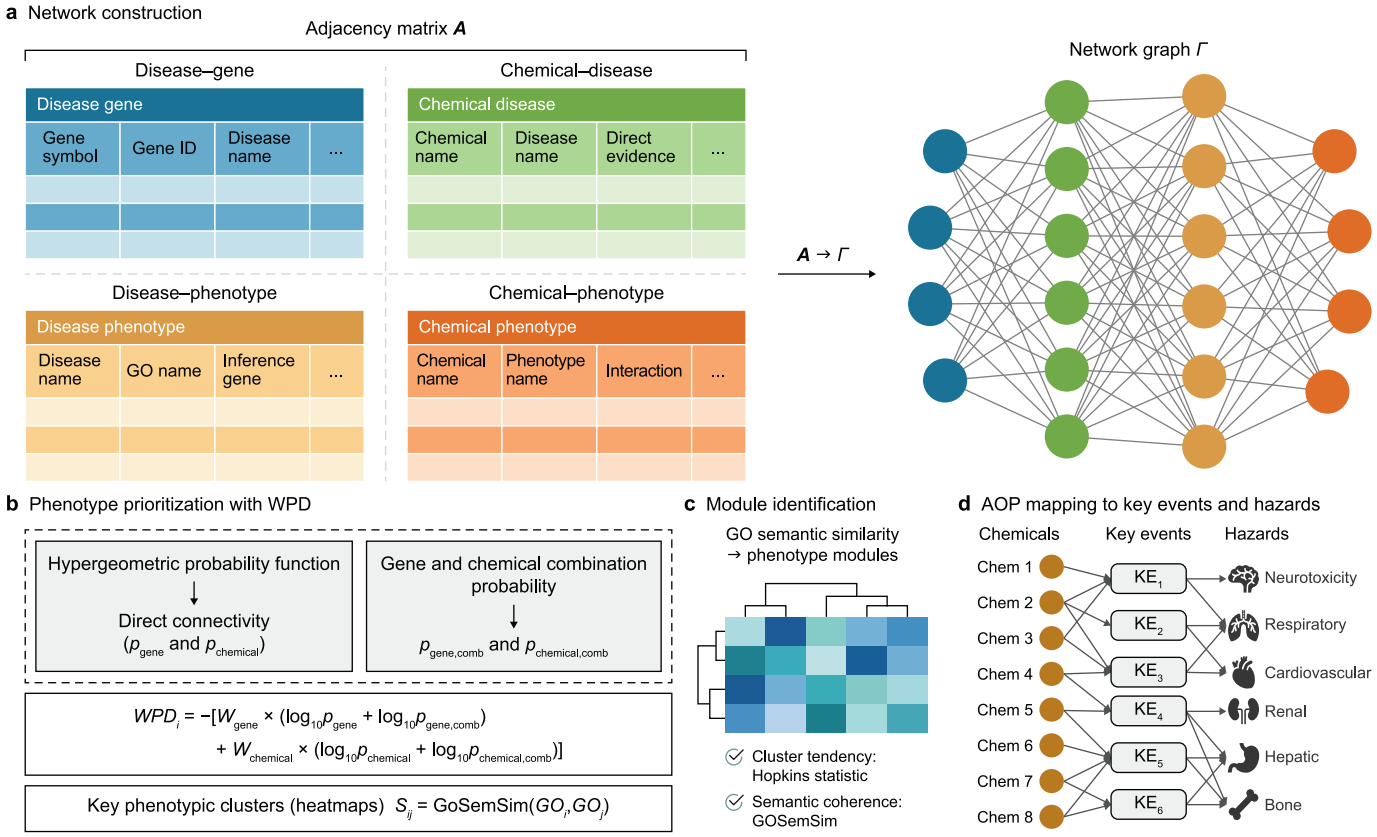

Fig. 1. Overall framework and workflow of the AOP-ExpoVis platform. a, Construction of a heterogeneous network from the Comparative Toxicogenomics Database, integrating chemicals, genes, phenotypes, and diseases, and the curated associations among them. **b,** Application of the weighted phenotype-disease (WPD) scoring algorithm that combines hypergeometric testing and network topology to calculate phenotypic significance scores, identifying key phenotypes associated with specific chemical-disease pairs while avoiding hub node bias. **c,** Identification of phenotype modules by clustering prioritized phenotypes based on Gene Ontology (GO) term semantic similarity, with cluster tendency and semantic coherence evaluated using the Hopkins statistic and GOSemSim. **d,** Mapping of phenotypic modules to key events in AOP-Wiki, connecting computational predictions with established toxicity pathways to generate testable mechanistic hypotheses.

3.3. Case study 1: phenotypic inference of BDE-47-induced neurodegenerative disorders

3.3.1. Phenotype-disease mapping and KE identification via AOP-ExpoVis

BDE-47 exposure was associated with 115 phenotypes in normal (non-tumor) tissues or cells, encompassing five neurodegenerative diseases. These conditions overlapped with 111 phenotypes, which were identified as potential KEs for BDE-47-induced pathogenesis. To refine these associations, phenotypes were prioritized based on significance via the inference network topology.

The WPD scores of the 111 overlapping phenotypes were calculated (Supplementary Table S3), followed by hierarchical clustering and heatmap visualization (Fig. 3a). Distinct shared phenotypic profiles were observed across diseases, indicating similar molecular associations with BDE-47. To characterize the KEs of BDE-47-induced neurodegeneration, the top 40% of phenotypes per disease (by WPD score) were selected (Supplementary Table S4). Cluster analysis of these high-priority phenotypes (Fig. 3b) revealed significant non-random aggregation ($H = 0.676$), and functional similarity analysis of this cluster demonstrated significant biological coherence. This supports the finding that BDE-47 may act through common neurobiological mechanisms, potentially perturbing lipid biosynthesis and glucose homeostasis—two processes critical to neurodegeneration [30–32].

Based on the phenotypes inferred for BDE-47-induced neurodegenerative disorders, AOP-ExpoVis mapped these to a total of 204 AOPs. Following functional relevance filtering, 32 AOPs were retained for further evaluation (Supplementary Table S5). Among these, four AOPs (Aop:152 (https://aopwiki.org/aops/152), Aop:500 (https://aopwiki.org/aops/500), Aop:458 ([https://aopwiki.org/aops/458], and Aop:13 [https://aopwiki.org/aops/13]) exhibited significant total scores and enrichment ratios (≥0.3). Therefore, they represent core pathways of BDE-47-induced neurotoxicity.

3.3.2. In vitro validation results of BDE-47-induced neurotoxicity

To elucidate the mechanisms underlying this toxicity, we focused on the MIE of AOP:458. This represents AhR activation in the liver, which drives adverse neurodevelopmental outcomes. AhR is a cytosolic protein that translocates to the nucleus upon ligand binding, heterodimerizes with AhR nuclear translocator, and binds dioxin/xenobiotic response elements [33]. As a lipophilic ligand, BDE-47 can cross the blood–brain barrier to affect brain physiology [34]. Prior studies have linked AhR activation to disrupted neuronal migration [35], impaired hippocampal differentiation and memory [36], dysregulated astrocyte and microglial function [37,38], and PBDE-induced neurodevelopmental damage [39–41], supporting the hypothesis that BDE-47 induces cognitive dysfunction via AhR activation. A mouse hippocampal neuronal HT22 cell model was established.

BDE-47 reduced HT22 cell viability in a dose–dependent manner (Supplementary Fig. S1a). Compared to controls,

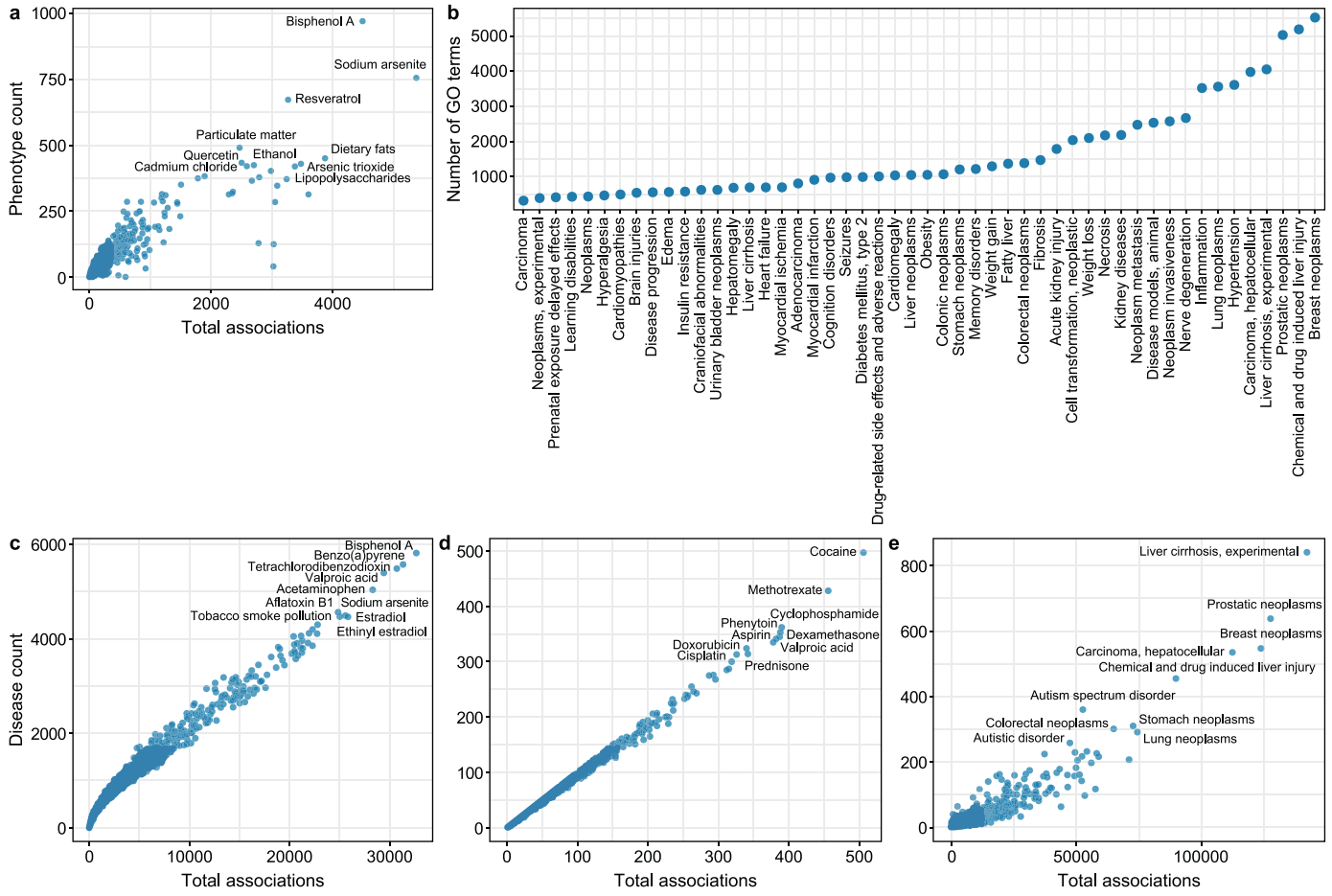

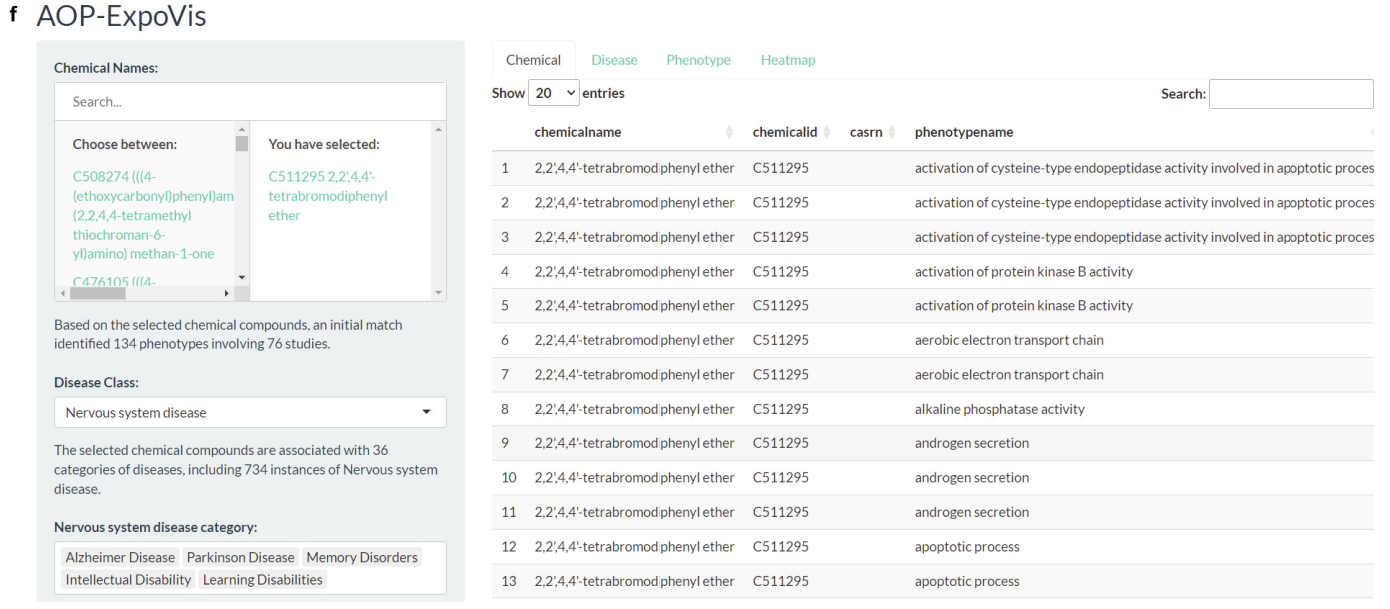

Fig. 2. Visualization of chemical–phenotype–disease associations and AOP-ExpoVis platform outputs. a, Distribution of chemical–phenotype associations versus phenotype counts, annotated with the top 10 chemicals exhibiting the highest phenotype diversity. **b,** Top 50 diseases ranked by number of associated Gene Ontology (GO) terms, reflecting functional diversity. **c,** Scatter plot of chemical–disease associations colored by interaction density, highlighting the top 10 chemicals with the highest disease counts. **d,** Scatter plot of curated high-confidence chemical–disease associations. **e,** Disease–gene association network highlighting the top 10 diseases with the most significant connections. **f,** Example AOP-ExpoVis query output displaying mapped phenotypes, diseases, and exposure–outcome relationships for specific chemicals.

viability decreased by 11.91–57.98% (all $P < 0.01$) at 2.5–160 μM. We therefore selected 2.5 μM (low), 5 μM (medium), and 10 μM (high) for subsequent experiments. CH-223191 (AhR inhibitor) had no significant effect on viability at 3–12 μM (Supplementary Fig. S1b), so 10 μM BDE-47 and 12 μM CH-223191 was used for cotreatment. Morphologically, 2.5 μM BDE-47 caused no obvious changes; 5 μM

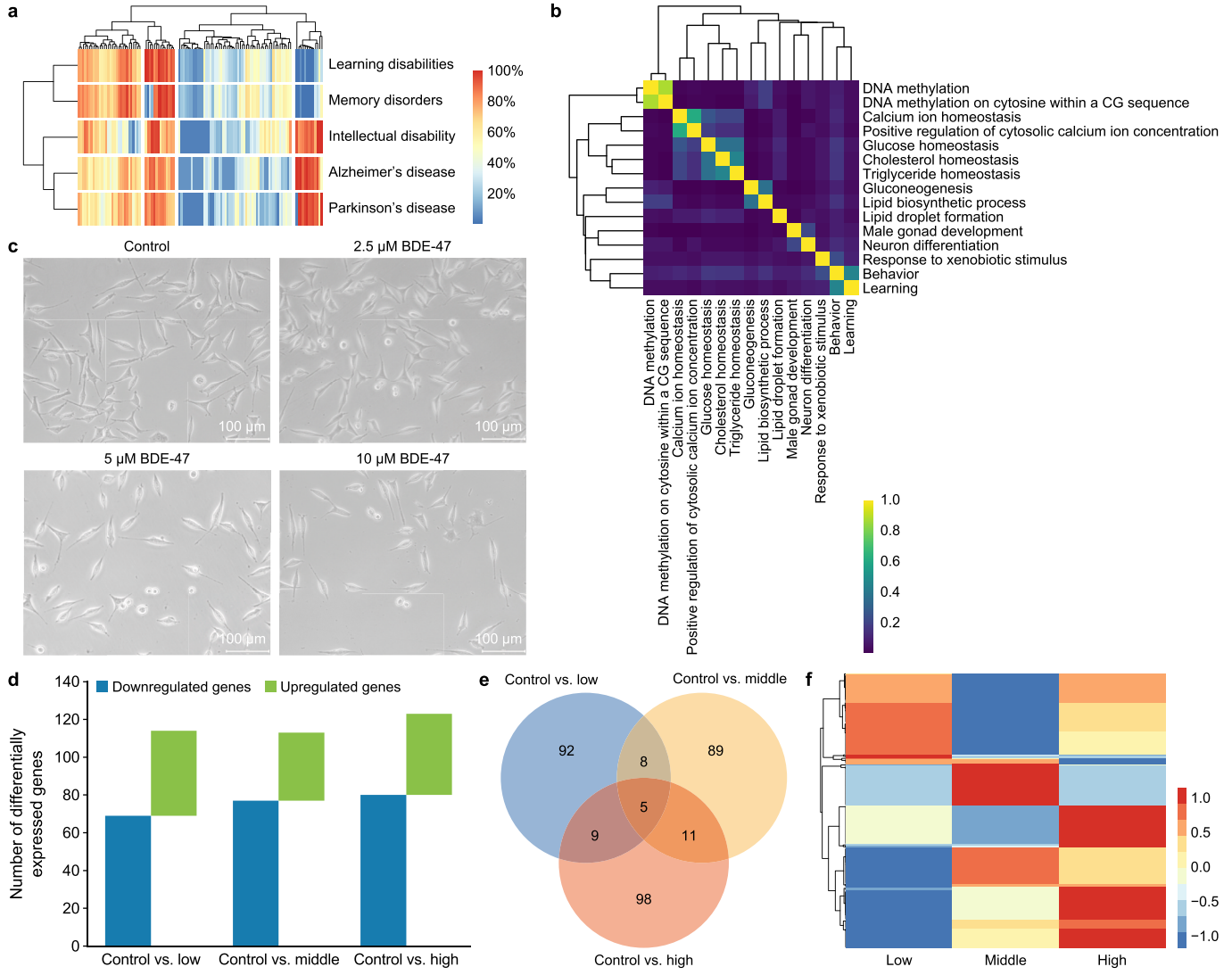

Fig. 3. Phenotypic inference by AOP-ExpoVis and in vitro validation of BDE-47-induced neurotoxicity. a, Heatmap with hierarchical clustering of shared phenotypes across neurodegenerative diseases (intellectual disability, Alzheimer's disease, Parkinson's disease, learning disabilities, memory disorders) associated with BDE-47 exposure. Generated via AOP-ExpoVis. **b,** Semantic similarity matrix of Gene Ontology (GO) terms for phenotypes, showing functional coherence of clustered phenotypes. Generated via AOP-ExpoVis. **c,** Morphological changes in HT22 cells under different concentrations of BDE-47 (Control; 2.5 μM BDE-47; 5 μM BDE-47; 10 μM BDE-47; 400 × magnification). **d,** Comparison of differentially expressed genes (DEGs) in the low (2.5 μM), medium (5 μM), and high (10 μM) treatment groups relative to the control group, showing the number of upregulated and downregulated genes. **e**, Venn diagram of DEGs across BDE-47 dose groups. **f**, Heatmap of DEGs, with the *x*-axis representing treatment groups and the *y*-axis representing individual genes. The color gradient (blue to red) indicates gene expression levels from low to high. **g–i,** Bubble plots of Kyoto Encyclopedia of Genes and Genomes (KEGG) pathway enrichment analysis for DEGs in low (**g**), medium (**h**), and high (**i**) dose groups. **j,** Venn diagram of KEGG pathway enrichment across dose groups, focusing on metabolism of xenobiotics by cytochrome P450. **k–l,** Reverse transcription quantitative polymerase chain reaction validation of *Gstp2* (**k**) and *Ugt2b34* (**l**) mRNA expression in HT22 cells ($n = 4$ per group) treated with 10 μM BDE-47, with or without AhR inhibitor CH-223191. *$P < 0.05$ vs. control group; ***$P < 0.001$ vs. control group; #$P < 0.05$ vs. 10 μM BDE-47 group; ##$P < 0.01$ vs. 10 μM BDE-47 group. **m,** Semantic similarity distribution between predicted phenotypes and GO terms from transcriptomic profiles. The histogram (gray) shows the frequency of semantic similarity values, and the red density curve indicates the distribution trend. The dashed line represents the validation threshold (semantic similarity ≥0.7).

reduced cell numbers and shortened synapses; and 10 μM induced marked cell loss, increased intercellular distance, and shrinkage (Fig. 3c), confirming dose-dependent cytotoxicity.

Transcriptomic sequencing was performed on HT22 cells treated with 2.5, 5, and 10 μM BDE-47 for 24 h. The quality of the RNA satisfied the criteria listed (Supplementary Table S6) (rRNA A260/280, A260/230 ratios, RIN values). Library integrity and uniform coverage were confirmed by the analyses presented (Supplementary Fig. S2). Sequencing results (Supplementary Table S7) indicated >90% read alignment to the reference genome and >70% unique mapping, ensuring high depth and reproducibility. DEG analysis revealed 114 (45 upregulated, 69 downregulated), 113 (36 upregulated, 77 downregulated), and 123 (43 upregulated, 80 downregulated) DEGs in the low-, medium-, and high-dose groups, respectively (Fig. 3d). A Venn diagram (Fig. 3e) and a heatmap (Fig. 3f) represented distinct expression patterns across doses, with more pronounced changes in the high-dose group. KEGG pathway enrichment analysis (Fig. 3g–i) identified "metabolism of xenobiotics by cytochrome P450" as significantly enriched in all dose groups (Fig. 3j). The CYP450 enzyme family catalyzes oxidative reactions [42], accounting for 70–80% of xenobiotic-metabolizing enzymes critical to drug

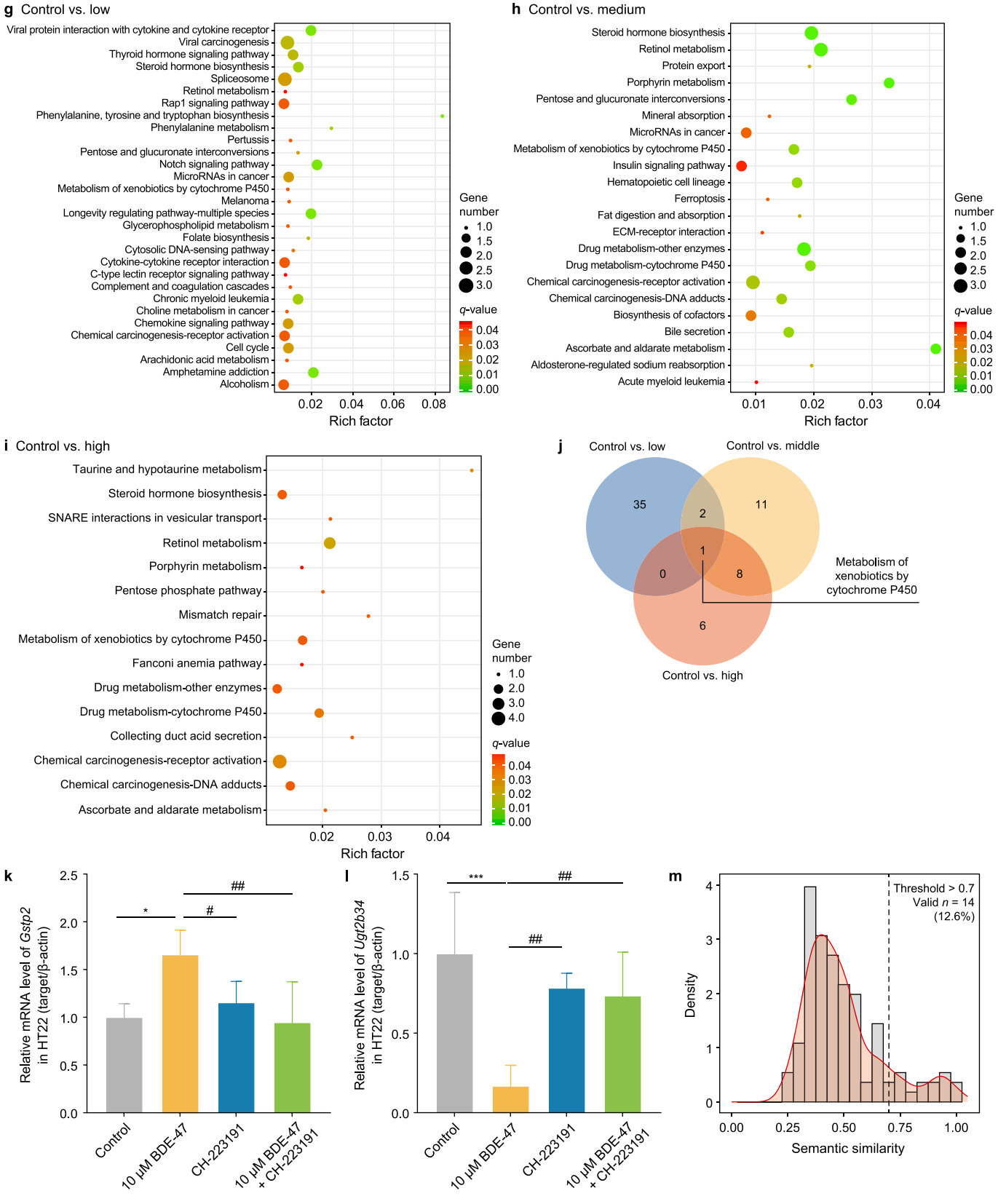

Fig. 3. (*continued*).

biotransformation [43,44], and it is involved in PBDE biotransformation, where it alters bioactivity and toxicity [45,46].

We validated two key genes (*Gstp2* and *Ugt2b34*) in this pathway. CH-223191 alone had no effect on their mRNA

expression, but 10 μM BDE-47 significantly upregulated *Gstp2* and downregulated *Ugt2b34* (both $P < 0.05$; Fig. 3k and l). Cotreatment with BDE-47 and CH-223191 partially reversed these changes ($P < 0.05$), indicating that AhR activation regulates *Gstp2/Ugt2b34* expression to affect HT22 cell metabolism. This is consistent with prior reports that AhR forms stable complexes with exogenous and endogenous molecules [47–50].

Integrating AOP-inferred phenotypic KEs with GO terms from the high-dose transcriptomic profile revealed significant concordance: 14 of the 111 predicted phenotypes (encompassing epigenetic regulation, calcium homeostasis, oxidative stress, and apoptosis) were recapitulated in exposed cells (semantic similarity >0.7) (Fig. 3m, Supplementary Table S4). This convergence validates the computational model and delineates a coherent mechanistic network underlying BDE-47-induced neuronal dysfunction.

3.4. Case study 2: phenotypic inference of arsenic-induced breast carcinogenesis

In this study, we screened 311 phenotypes associated with arsenic exposure and focused on four breast cancer types: breast neoplasms (D001943), inflammatory breast neoplasms (D058922), triple negative breast neoplasms (D064726), and carcinoma, ductal, breast (D018270). The analysis identified 246 phenotypes that overlapped between these four breast cancers and arsenic exposure, suggesting their potential role as KEs in arsenic-induced pathogenesis. To precisely characterize the phenotype–disease associations implicated in these mechanisms, we prioritized the phenotypes based on network topology and performed cluster analysis and heatmap visualization using the WPD scores of the overlapping phenotypes (Fig. 4a, Supplementary Table S8). The results revealed that these breast cancer types share distinct phenotypic profiles.

In subsequent characterization, we selected the top 20% of phenotypes with the highest WPD scores for each disease for further analysis (Fig. 4b, Supplementary Table S9). Cluster analysis of these high-priority phenotypes demonstrated a significant tendency toward clustering ($H = 0.631$), indicating an underlying common biological function. This observation suggests, at a mechanistic level, that arsenic-induced breast carcinogenesis may operate through shared oncogenic pathways, particularly by disrupting DNA damage response and cell cycle control, and by altering homeostasis of programmed cell death—two critical processes in tumorigenesis.

The AOP-ExpoVis analysis of arsenic and breast cancer revealed connections to 180 potential AOPs. After applying functional relevance filtering, 25 AOPs were selected for detailed analysis. From these, the five AOPs with the highest enrichment scores (AOP: 57 [https://aopwiki.org/aops/57], AOP: 60 [https://aopwiki.org/aops/60], AOP: 505 [https://aopwiki.org/aops/505], AOP: 139 [https://aopwiki.org/aops/139], and AOP: 141 [https://aopwiki.org/aops/141]) were postulated as core mechanisms of arsenic-induced breast cancer toxicity (Supplementary Table S10). Notably, AOP:57—which features activation of the AhR as the MIE—ranked highest. This corroborates King et al.'s earlier inference that GO term enrichment of chemical–disease associated genes implicates AhR in arsenic-related breast carcinogenesis. However, whereas their approach was confined to the AhR signaling pathway, the AOP-ExpoVis platform not only confirmed this pathway as top-ranked but also uncovered a broader array of candidate pathways, thereby expanding the mechanistic landscape of arsenic-induced breast cancer. This multi-pathway perspective better reflects the established notion that environmental pollutants often act through diverse biological routes to influence disease outcomes.

Notably, AOP:60—the second most highly enriched AOP identified here—implicates the pregnane X receptor (PXR), a nuclear receptor with recognized roles in cancer [51]. Although arsenic-induced AhR activation has been documented in carcinogenesis [52,53], and both PXR and AhR are known as key regulators of xenobiotic metabolism [54], no direct role for arsenic in PXR-mediated breast cancer risk has been experimentally established. Given arsenic's endocrine-disrupting properties, its potential activity via PXR activation presents a biologically plausible yet unexplored mechanism.

3.5. Case study 3: phenotypic inference in PFAS-induced liver disorders

Our analysis identified 286 and 240 phenotypes demonstrating significant associations with PFOA and PFOS exposure, respectively. We focused on five major liver disorders: liver diseases (D008107), liver cirrhosis (D008103), hepatitis (D006505), fatty liver (D005234), and non-alcoholic fatty liver disease (D065626). Phenotypic intersection analysis revealed 207 (PFOA) and 213 (PFOS) phenotypes shared with these hepatic conditions, which are proposed as potential KEs in PFAS-induced liver pathophysiology (Supplementary Tables S11–S12). To clarify phenotype–disease relationships, a network topology-based prioritization approach was applied. The WPD scores of overlapping phenotypes were subjected to cluster analysis and heatmap visualization, demonstrating that these liver disorders exhibit characteristic phenotypic signatures with substantial commonalities (Fig. 4c and d). Further investigation focused on the top 30% most significant phenotypes based on WPD scores for each condition. Cluster analysis of these high-priority phenotypes revealed strong clustering ($H = 0.785$ for PFOA and 0.753 for PFOS), supporting the existence of convergent biological mechanisms (Fig. 4e and f, Supplementary Tables S13–S14).

Using the AOP-ExpoVis platform, PFOA and PFOS were linked to 251 and 266 AOPs, respectively, via shared phenotypes, with 57 (PFOA) and 87 (PFOS) AOPs exhibiting significant enrichment. Key liver injury-related AOPs were identified: Aop:60 (https://aopwiki.org/aops/60), Aop:377 (https://aopwiki.org/aops/377), Aop:57 (https://aopwiki.org/aops/57), Aop:58 (https://aopwiki.org/aops/58), and Aop:529 (https://aopwiki.org/aops/529) (PFOA) (Supplementary Table S15); as well as Aop:57, Aop:58, Aop:60, Aop:494 (https://aopwiki.org/aops/494), and Aop:123 (https://aopwiki.org/aops/123) (PFOS) (Supplementary Table S16).

The study indicates that both PFAS compounds can disrupt liver homeostasis through coordinated pathogenic pathways. Specifically, PFOA primarily induces liver injury via the Aop:60 pathway, which involves PXR/SXR receptor activation leading to lipid metabolism disruption, and via the Aop:377 pathway, which mediates immune activation and triggers inflammatory responses. In contrast, PFOS acts mainly through the Aop:57 pathway initiated by AhR activation, promoting lipid accumulation, and the Aop:58 pathway, which disrupts lipid metabolism balance via multiple nuclear receptors. Their mechanistic profiles exhibit significant commonalities, such as shared lipid metabolism disruption pathways represented by Aop:57 and Aop:58, as well as chemical-specific mechanisms, such as the inflammation-related Aop:377 (which is uniquely associated with PFOA), indicating both overlapping and distinct pathogenic characteristics.

To experimentally validate the aforementioned phenotypic network and AOP inferences, we analyzed an independent GEO transcriptomic dataset. For PFOA, the analysis began with rigorous quality control. Principal component analysis (PCA) revealed a clear separation between the exposure and control groups along PC1, with good intragroup clustering (Supplementary Fig. S3a).

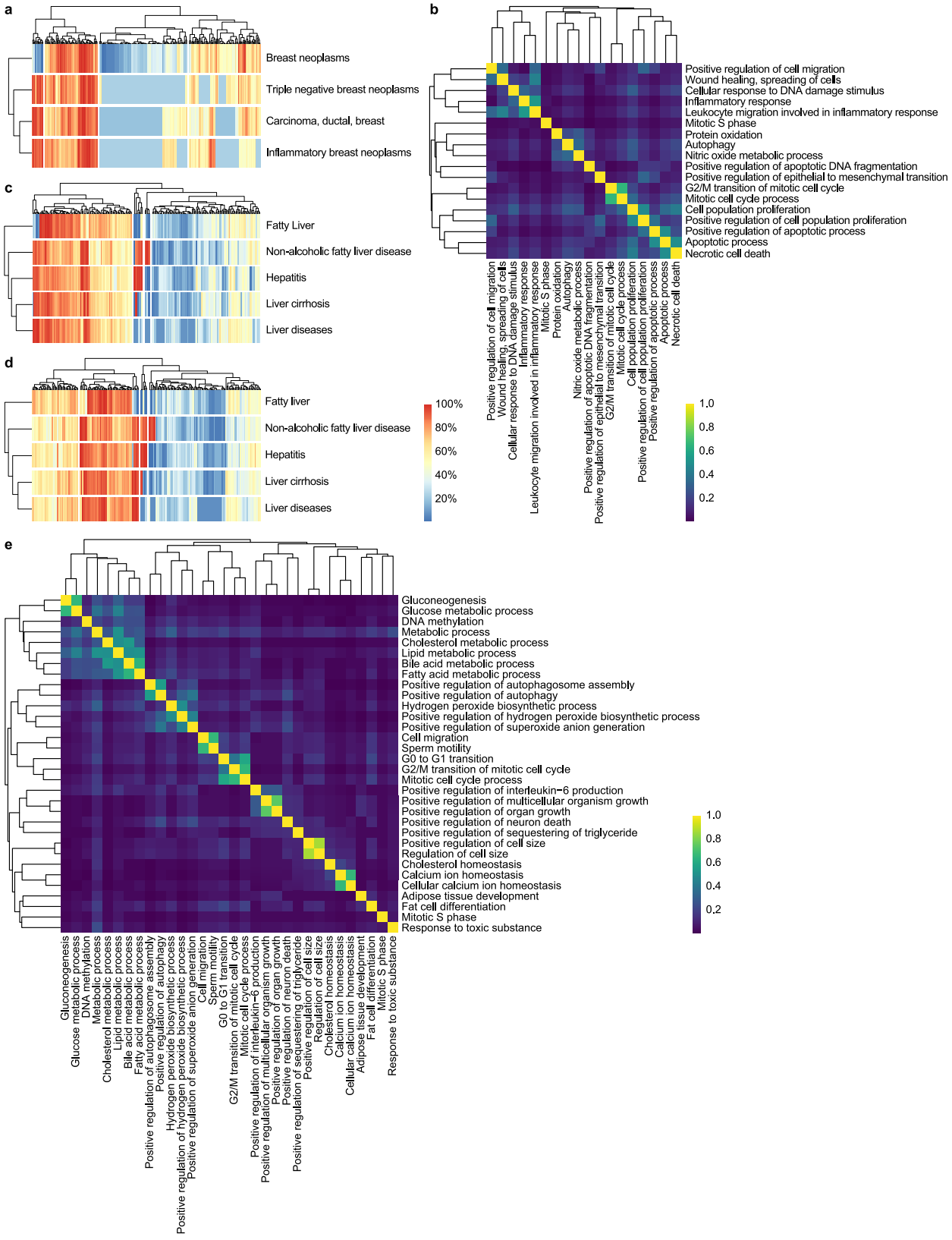

Fig. 4. Phenotypic inference of arsenic-induced breast carcinogenesis and PFAS-induced liver disorders via AOP-ExpoVis. a, Hierarchical heatmap of weighted phenotype-disease (WPD)-ranked shared phenotypes between arsenic and breast cancer subtypes (inflammatory, triple negative, ductal, breast neoplasms). **b,** Gene Ontology (GO) semantic similarity matrix for arsenic-breast cancer phenotypes, demonstrating functional coherence of clusters. **c,** Hierarchical heatmap of WPD-ranked shared phenotypes between perfluorooctanoic acid (PFOA) and liver diseases (cirrhosis, hepatitis, fatty liver, non-alcoholic fatty liver disease [NAFLD]). **d,** Hierarchical heatmap of WPD-ranked shared phenotypes between PFOS and liver diseases (cirrhosis, hepatitis, fatty liver, NAFLD). **e,** GO semantic similarity matrix for PFOA-liver disease phenotypes, illustrating functional convergence. **f,** GO semantic similarity matrix for PFOS-liver disease phenotypes, demonstrating pathway coherence. **g–h,** Semantic similarity distribution between predicted phenotypes and transcriptomic GO terms for PFOA (**g**) and perfluorooctane sulfonate (PFOS, **h**), with dashed line indicating validation threshold ($\geq$0.7). All heatmaps in this figure were generated within the AOP-ExpoVis platform.

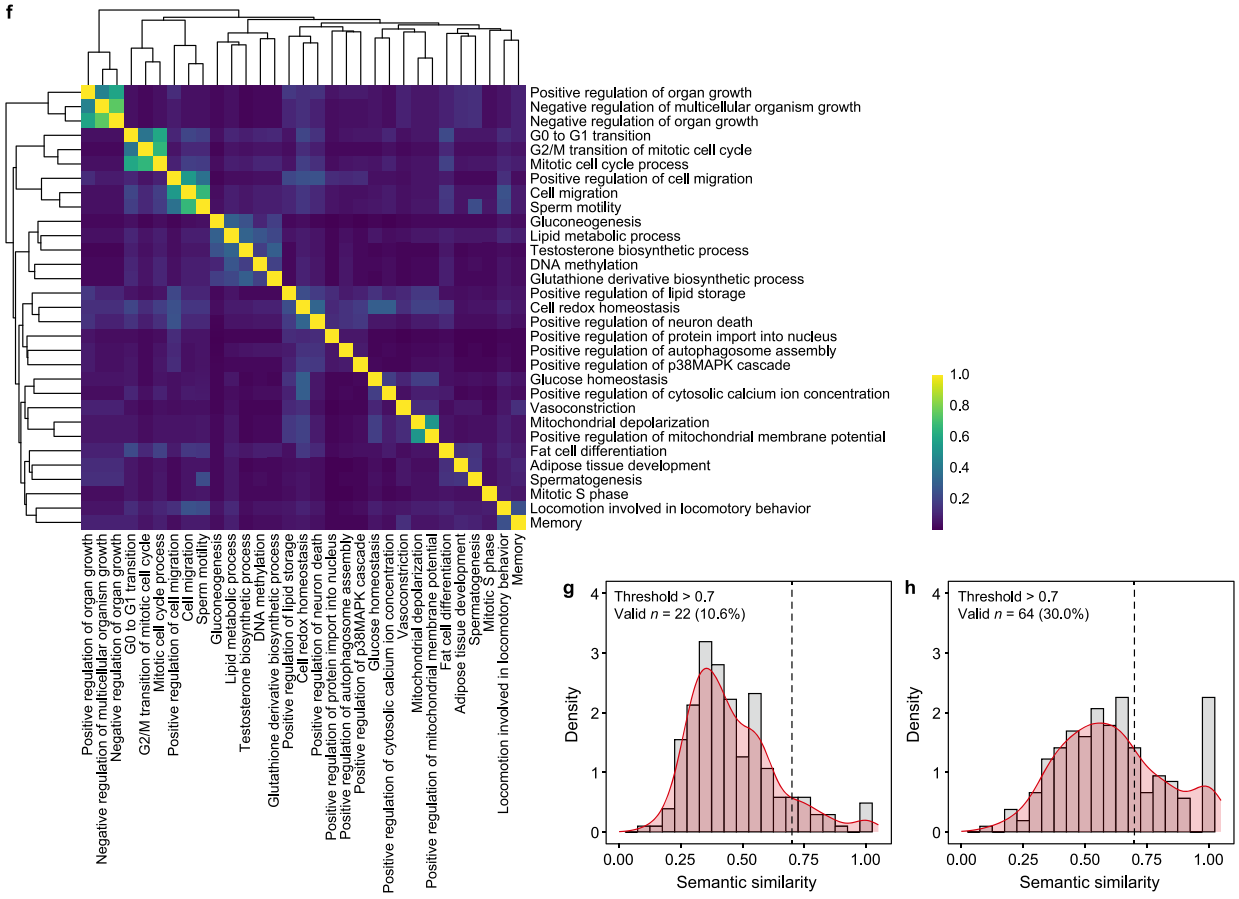

Fig. 4. (*continued*).

Boxplots of gene expression abundance confirmed the reliability of the data normalization process (Supplementary Fig. S3b), and a heatmap of the top 50 most significant DEGs further corroborated the distinct transcriptomic profile (Supplementary Fig. S3c). Differential expression analysis revealed that PFOA exposure induced significant expression changes in 698 genes (370 upregulated, 328 downregulated) (Supplementary Fig. S3d). Functional enrichment analysis of the upregulated genes revealed its distinct toxic mechanisms: GO analysis indicated significant enrichment in biological processes such as synaptic organization, regulation of cell adhesion, and ERK/NF-κB signaling pathways (Supplementary Fig. S3e), while KEGG analysis highlighted pathways involved in cell adhesion and migration, intracellular signal transduction, and immune–inflammatory responses (Supplementary Fig. S3f).

For PFOS, we applied a parallel analytical workflow. Similarly, PCA demonstrated clear separation from the control group (Supplementary Fig. S4a), normalized gene expression abundance was verified (Supplementary Fig. S4b), and a heatmap of the top 50 DEGs confirmed a distinct transcriptional signature (Supplementary Fig. S4c). PFOS exposure affected 697 genes (294 upregulated, 403 downregulated) (Supplementary Fig. S4d). Functional enrichment analysis of the upregulated genes suggested a different pattern: GO analysis was primarily associated with sterol or cholesterol metabolic processes and phospholipid metabolism (Supplementary Fig. S4e), while KEGG analysis demonstrated significant enrichment in lipid and fatty acid metabolism, central energy metabolism, and metabolic–inflammatory interactions (Supplementary Fig. S4f). These findings collectively indicate that PFOA and PFOS induce toxic effects through distinct molecular mechanisms. PFOA primarily affects cell communication and signal transduction, while PFOS markedly disrupts hepatic lipid homeostasis and core metabolic processes.

A cross-validation analysis was performed to align the phenotypic KEs inferred using AOP with the transcriptomic GO profiles from the GEO dataset, demonstrating significant concordance between the computational predictions and the empirical evidence. Specifically, 22 of the 207 phenotypes for PFOA (Fig. 4g, Supplementary Table S13) and 64 of the 213 for PFOS (Fig. 4h, Supplementary Table S14) were recapitulated in the exposed liver models (semantic similarity >0.7). The validated PFOA phenotypes revealed predominant enrichment in inflammatory and immune responses—including leukocyte migration involved in inflammatory response and T cell proliferation—along with fundamental cellular processes, such as cell population proliferation and apoptosis. In striking contrast, the extensively validated PFOS network highlighted comprehensive disruption of lipid and metabolic homeostasis, encompassing fatty acid homeostasis, cholesterol biosynthesis processes, triglyceride metabolic processes, and lipid catabolic processes. This clear mechanistic divergence—where PFOA primarily drives inflammation and proliferation, while PFOS orchestrates broad rewiring of hepatic metabolism—provides compelling molecular evidence for their distinct pathogenic roles in liver injury while robustly validating the respective AOP networks.

Based on external validation data, PFOA shows phenotypic characteristics dominated by inflammatory and immune responses, in stark contrast to the comprehensive lipid metabolic disruption observed in PFOS. These independent data are highly

consistent with our predictions from the AOP-ExpoVis platform. The prominent inflammatory and immune phenotypes of PFOA directly confirm the critical role of the Aop:377 pathway predicted by the platform, while the extensive lipid metabolic dysregulation exhibited by PFOS strongly supports the central importance of the platform-identified Aop:57 and Aop:58 pathways. This strong concordance between the external data and the platform's predictions strikingly confirms the excellent accuracy and robustness of the AOP-ExpoVis platform in identifying chemical toxicity mechanisms. A notable observation from the integrated validation was that PFOS demonstrated a higher phenotype recapitulation rate than PFOA. We propose that this may occur because PFOS-induced hepatotoxicity mechanisms are highly concentrated within the domain of lipid and metabolic homeostasis. This biological domain benefits from a particularly well-defined and structurally comprehensive GO namespace [55], which likely facilitates more robust semantic matching. This observation leads to a testable hypothesis: the semantic organization and clarity of a biological domain itself may influence computational recapitulation efficacy, a possibility that merits further study.

3.6. Synthesis of AOP-ExpoVis platform capabilities across all case studies

AOP-ExpoVis establishes a predictive toxicological framework through systematic phenotype–disease mapping, network topology-based prioritization, and AOP association and pathway enrichment analysis. Its predictive capability was rigorously validated across three independent case studies, each designed to minimize bias and ensure objective assessment. In Case 1 (BDE47), the platform-identified MIE of AOP:458—AhR activation—was experimentally validated using a self-constructed in vitro neuronal model. Transcriptomic and functional assays confirmed AhR activation and elucidated downstream KEs, including the enrichment of the “metabolism of xenobiotics by cytochrome P450” pathway and the regulation of *Gstp2* and *Ugt2b34*, thereby closing the mechanistic loop from prediction to physiological outcome. In Case 2 (arsenic), AOP-ExpoVis recapitulated previously established mechanisms—such as AhR activation (AOP:57)—and proposed novel plausible pathways, including PXR-mediated signaling (AOP:60), thereby extending the field's current understanding of arsenic-induced breast carcinogenesis. In Case 3 (PFAS), the platform's predictions demonstrated strong concordance with an independent public transcriptomic dataset. It successfully discriminated between PFOA-driven inflammatory and immune phenotypes (Aop:377) and PFOS-specific disruptions in lipid and metabolic homeostasis (Aop:57 and Aop:58), highlighting its ability to capture compound-specific toxicodynamic profiles. Critically, throughout all cases, computational predictions and experimental validation were conducted independently and in parallel. This deliberate separation ensured that the validation process remained unbiased, thereby robustly affirming the predictive power and translational relevance of the AOP-ExpoVis platform in mechanistically informed chemical safety assessment.

3.7. Limitations of the AOP-ExpoVis platform

Although the AOP-ExpoVis platform has demonstrated promising predictive capabilities across multiple case studies, several limitations remain and should be addressed in future work. First, the platform's reliance on existing knowledge bases, such as AOP-Wiki and CTD, inherently constrains its predictive scope. Although systematic inferences were established through phenotypic networks, the predicted chemical–phenotype–AOP associations should be regarded as well-founded hypotheses rather than definitive conclusions without experimental validation. Second, the phenotype–KE mapping strategy prioritizes accuracy by including only KEs with standardized annotations. While this approach ensures reproducibility, it may exclude biologically relevant KEs that have not yet been formally annotated. Future advances in knowledge representation and natural language processing could help expand coverage while maintaining reliability. Third, the computational framework's quantitative capabilities and benchmarking require further development. Current predictions rely primarily on qualitative or semi-quantitative methods, such as topological sorting and enrichment analysis. The platform has yet to incorporate advanced machine learning models or kinetic parameters, which would enable it to quantitatively estimate pathway activation strength or the likelihood of adverse outcomes. Moreover, although multiple case studies support its utility, systematic performance comparisons with existing tools remain limited. Future efforts should establish standardized benchmark datasets and adopt quantitative metrics to more objectively demonstrate the platform's advantages. Finally, the current version focuses mainly on single-chemical exposures and linear pathways. To address this limitation, future developments could expand the platform to accommodate more complex scenarios, including mixture toxicity, chronic low-dose effects, and host susceptibility factors, thereby enhancing its relevance to real-world toxicological assessment.

4. Conclusion

This study establishes AOP-ExpoVis as a powerful, integrative tool for toxicological research that supports data integration, visualization, and analysis (Supplementary Table S17) [13,56,57]. A key innovation is the WPD scoring system, which reduces hub bias in large-scale networks and prioritizes phenotypes that are mechanistically relevant to chemical toxicity. By linking gene, chemical, phenotype, and disease networks, AOP-ExpoVis enables the identification of KEs and maps these to curated pathways in AOP-Wiki, providing a systematic framework for mechanistic inference.

Through three independent case studies involving BDE-47, arsenic, and PFAS, we demonstrate that AOP-ExpoVis consistently predicts chemical-specific toxicity pathways. For BDE-47, the platform identified AhR activation as a critical MIE, which was experimentally validated in neuronal cells. For arsenic, it recapitulated known AhR-mediated breast carcinogenicity and uncovered a novel role for PXR signaling. For PFAS, it discriminated between PFOA-driven inflammation and PFOS-induced lipid metabolic disruption, with predictions supported by external transcriptomic data.

Collectively, these findings highlight the platform's ability to support chemical prioritization and enhance hazard assessment by providing mechanistically informed insights into chemical toxicity.

CRediT authorship contribution statement

Huajie Yang: Writing - Original Draft, Software, Methodology, Investigation, Data Curation, Conceptualization, Writing - Review & Editing, Validation. **Kaiyi Zhang:** Writing - Original Draft, Methodology. **Yue Wang:** Visualization. **Shuailing Liu:** Methodology. **Yinchu Guo:** Software. **Wei Liu:** Investigation. **Jiaxing Sun:** Methodology. **Zhaoqi Zhang:** Data Curation. **Sen Zhang:** Methodology. **Shenghang Li:** Methodology. **Yingcheng Zhao:** Data Curation. **Tong Liu:** Data Curation. **Junhong Liu:** Data Curation. **Liang Pei:** Data Curation. **Shuhua Xi:** Funding Acquisition, Data curation, Conceptualization, Project Administration. **Peng Shi:** Writing - Review & Editing, Supervision, Methodology, Funding Acquisition, Formal Analysis, Conceptualization.

Declaration of competing interest

The authors declare that they have no known competing financial interests or personal relationships that could have appeared to influence the work reported in this paper.

Acknowledgements

We would like to acknowledge the valuable resources provided by the Comparative Toxicogenomics Database and the Adverse Outcome Pathway Wiki. The work was supported by the National Natural Science Foundation of China (Grant No. 42407576), the National Key Research and Development Program of China (Grant No. 2018YFC1801204), the China Postdoctoral Science Foundation (Grant No. 2025T180209), the China Postdoctoral Science Foundation (No. 2023MD744265) and the National Funded Postdoctoral Fellowship Program (No. GZC20233119).

Appendix A. Supplementary data

Supplementary data to this article can be found online at https://doi.org/10.1016/j.ese.2026.100663.

References

[1] Z. Wang, G.W. Walker, D.C.G. Muir, et al., Toward a global understanding of chemical pollution: a first comprehensive analysis of national and regional chemical inventories, Environ. Sci. Technol. 54 (5) (2020) 2575, https://doi.org/10.1021/acs.est.9b06379.
[2] F. Wang, L. Xiang, K. Sze-Yin Leung, et al., Emerging contaminants: a one health perspective, Innovation 5 (4) (2024) 100612, https://doi.org/10.1016/j.xinn.2024.100612.
[3] D.J. Carlin, C.V. Rider, Combined exposures and mixtures research: an enduring NIEHS priority, Environ. Health Perspect. 132 (7) (2024) 75001, https://doi.org/10.1289/EHP14340.
[4] N. Delrue, M. Sachana, Y. Sakuratani, et al., The adverse outcome pathway concept: a basis for developing regulatory decision-making tools, Altern. Lab. Anim. 44 (5) (2016) 417, https://doi.org/10.1177/026119291604400504.
[5] G.T. Ankley, S.W. Edwards, The adverse outcome pathway: a multifaceted framework supporting 21(st) century toxicology, Curr Opin Toxicol 9 (2018) 1, https://doi.org/10.1016/j.cotox.2018.03.004.
[6] G. Del Giudice, A. Serra, A. Pavel, et al., A network toxicology approach for mechanistic modelling of nanomaterial hazard and adverse outcomes, Adv. Sci. (Weinh.) 11 (32) (2024) e2400389, https://doi.org/10.1002/advs.202400389.
[7] J.J. Sutherland, Y.W. Webster, J.A. Willy, et al., Toxicogenomic module associations with pathogenesis: a network-based approach to understanding drug toxicity, Pharmacogenomics J. 18 (3) (2018) 377, https://doi.org/10.1038/tpj.2017.17.
[8] M. Huang, A. Bargues-Carot, Z. Riaz, et al., Impact of environmental risk factors on mitochondrial dysfunction, neuroinflammation, protein misfolding, and oxidative stress in the etiopathogenesis of parkinson's disease, Int. J. Mol. Sci. 23 (18) (2022), https://doi.org/10.3390/ijms231810808.
[9] C.P. Wild, Complementing the genome with an "exposome": the outstanding challenge of environmental exposure measurement in molecular epidemiology, Cancer Epidemiol. Biomarkers Prev. 14 (8) (2005) 1847, https://doi.org/10.1158/1055-9965.EPI-05-0456.
[10] R. Barouki, K. Audouze, C. Becker, et al., The exposome and toxicology: a win-win collaboration, Toxicol. Sci. 186 (1) (2022) 1, https://doi.org/10.1093/toxsci/kfab149.
[11] A.L. Foreman, B. Warth, E.V.S. Hessel, et al., Adopting mechanistic molecular biology approaches in exposome research for causal understanding, Environ. Sci. Technol. 58 (17) (2024) 7256, https://doi.org/10.1021/acs.est.3c07961.
[12] P. Langfelder, S. Horvath, WGCNA: an R package for weighted correlation network analysis, BMC Bioinf. 9 (2008) 559, https://doi.org/10.1186/1471-2105-9-559.
[13] A.P. Davis, T.C. Wiegers, D. Sciaky, et al., Comparative Toxicogenomics Database's 20th anniversary: update 2025, Nucleic Acids Res. 53 (D1) (2025) D1328, https://doi.org/10.1093/nar/gkae883.
[14] M. Liu, Z. Yu, Z. Zhao, et al., MiR-24-3p/Dio3 axis is essential for BDE47 to induce local thyroid hormone disorder and neurotoxicity, Toxicology 491 (2023) 153527, https://doi.org/10.1016/j.tox.2023.153527.
[15] N. Khanjani, A.B. Jafarnejad, L. Tavakkoli, Arsenic and breast cancer: a systematic review of epidemiologic studies, Rev. Environ. Health 32 (3) (2017) 267, https://doi.org/10.1515/reveh-2016-0068.
[16] X. Du, D.L. Li, X. Xu, et al., Effects of mixed exposure to PFAS on adolescent non-alcoholic fatty liver disease: integrating evidence from human cohorts, toxicogenomics, and animal models to uncover mechanisms and potential target sites, J. Hazard Mater. 485 (2025) 136854, https://doi.org/10.1016/j.jhazmat.2024.136854.
[17] G. Yu, Gene ontology semantic similarity analysis using GOSemSim, Methods Mol. Biol. 2117 (2020) 207, https://doi.org/10.1007/978-1-0716-0301-7_11.
[18] G. Yu, F. Li, Y. Qin, et al., GOSemSim: an R package for measuring semantic similarity among GO terms and gene products, Bioinformatics 26 (7) (2010) 976, https://doi.org/10.1093/bioinformatics/btq064.
[19] H. Frohlich, N. Speer, A. Poustka, et al., GOSim–an R-package for computation of information theoretic GO similarities between terms and gene products, BMC Bioinf. 8 (2007) 166, https://doi.org/10.1186/1471-2105-8-166.
[20] H. Tominaga, M. Ishiyama, F. Ohseto, et al., A water-soluble tetrazolium salt useful for colorimetric cell viability assay 36 (2) (1999) 47.
[21] J.Z. Wang, Z. Du, R. Payattakool, et al., A new method to measure the semantic similarity of GO terms, Bioinformatics 23 (10) (2007) 1274, https://doi.org/10.1093/bioinformatics/btm087.
[22] B.L. King, A.P. Davis, M.C. Rosenstein, et al., Ranking transitive chemical-disease inferences using local network topology in the comparative toxicogenomics database, PLoS One 7 (11) (2012) e46524, https://doi.org/10.1371/journal.pone.0046524.
[23] Y. Wang, Z. Zhu, L. Deng, et al., Multiscale synergy networks offer insights into disease and comorbidity mechanisms, Anal. Chem. (2025), https://doi.org/10.1021/acs.analchem.4c06133.
[24] J. Kim, K.A. Do, M.J. Ha, et al., Bayesian inference of hub nodes across multiple networks, Biometrics 75 (1) (2019) 172, https://doi.org/10.1111/biom.12958.
[25] S. Mukherjee, T.P. Speed, Network inference using informative priors, Proc. Natl. Acad. Sci. U. S. A. 105 (38) (2008) 14313, https://doi.org/10.1073/pnas.0802272105.
[26] D. Yang, X. Zhu, C. Yan, et al., Joint hub identification for brain networks by multivariate graph inference, Med. Image Anal. 73 (2021) 102162, https://doi.org/10.1016/j.media.2021.102162.
[27] M.A. Kamat, J.A. Blackshaw, R. Young, et al., PhenoScanner V2: an expanded tool for searching human genotype-phenotype associations, Bioinformatics 35 (22) (2019) 4851, https://doi.org/10.1093/bioinformatics/btz469.
[28] Y. Lu, S. Liu, Y. Sun, et al., Identification of key genes in hepatocellular carcinoma associated with exposure to TCDD and alpha-endosulfan by WGCNA, Ecotoxicol. Environ. Saf. 252 (2023) 114595, https://doi.org/10.1016/j.ecoenv.2023.114595.
[29] Z. Chai, C. Zhao, Y. Jin, et al., Generating adverse outcome pathway (AOP) of inorganic arsenic-induced adult male reproductive impairment via integration of phenotypic analysis in comparative toxicogenomics database (CTD) and AOP wiki, Toxicol. Appl. Pharmacol. 411 (2021) 115370, https://doi.org/10.1016/j.taap.2020.115370.
[30] M. Casella, G. Lori, L. Coppola, et al., BDE-47, -99, -209 and their ternary mixture disrupt glucose and lipid metabolism of Hepg2 cells at dietary relevant concentrations: mechanistic insight through integrated transcriptomics and proteomics analysis, Int. J. Mol. Sci. 23 (22) (2022), https://doi.org/10.3390/ijms232214465.
[31] H. He, X. Shi, A. Lawrence, et al., 2,2',4,4'-tetrabromodiphenyl ether (BDE-47) induces wide metabolic changes including attenuated mitochondrial function and enhanced glycolysis in PC12 cells, Ecotoxicol. Environ. Saf. 201 (2020) 110849, https://doi.org/10.1016/j.ecoenv.2020.110849.
[32] S. Bloch, L. Lévêque, I. Hertz-Picciotto, et al., Using in vitro data to derive acceptable exposure levels: a case study on PBDE developmental neurotoxicity, Environ. Int. 183 (2024) 108411, https://doi.org/10.1016/j.envint.2023.108411.
[33] X. Diao, Q. Shang, M. Guo, et al., Structural basis for the ligand-dependent activation of heterodimeric AHR-ARNT complex, Nat. Commun. 16 (1) (2025) 1282, https://doi.org/10.1038/s41467-025-56574-7.
[34] L. Sládeková, S. Mani, Z. Dvořák, Ligands and agonists of the aryl hydrocarbon receptor AhR: facts and myths, Biochem. Pharmacol. 213 (2023) 115626, https://doi.org/10.1016/j.bcp.2023.115626.
[35] D.A. Keays, G. Tian, K. Poirier, et al., Mutations in alpha-tubulin cause abnormal neuronal migration in mice and lissencephaly in humans, Cell 128 (1) (2007) 45, https://doi.org/10.1016/j.cell.2006.12.017.
[36] S.E. Latchney, A.M. Hein, M.K. O'Banion, et al., Deletion or activation of the aryl hydrocarbon receptor alters adult hippocampal neurogenesis and contextual fear memory, J. Neurochem. 125 (3) (2013) 430, https://doi.org/10.1111/jnc.12130.
[37] N.A. Ramos-García, M. Orozco-Ibarra, E. Estudillo, et al., Aryl hydrocarbon receptor in post-mortem hippocampus and in serum from young, elder, and alzheimer's patients, Int. J. Mol. Sci. 21 (6) (2020), https://doi.org/10.3390/ijms21061983.
[38] V. Rothhammer, D.M. Borucki, E.C. Tjon, et al., Microglial control of astrocytes in response to microbial metabolites, Nature 557 (7707) (2018) 724, https://doi.org/10.1038/s41586-018-0119-x.
[39] B. Das, K. Okamoto, J. Rabalais, et al., Congenital tufting enteropathy-associated mutant of epithelial cell adhesion molecule activates the unfolded protein response in a murine model of the disease, Cells 9 (4) (2020), https://doi.org/10.3390/cells9040946.
[40] J. Tang, B. Hu, H. Zheng, et al., 2,2',4,4'-Tetrabromodiphenyl ether (BDE-47) activates Aryl hydrocarbon receptor (AhR) mediated ROS and NLRP3 inflammasome/p38 MAPK pathway inducing necrosis in cochlear hair cells, Ecotoxicol. Environ. Saf. 221 (2021) 112423, https://doi.org/10.1016/j.ecoenv.2021.112423.

[41] J. Yuan, X. Sun, S. Che, et al., AhR-mediated CYP1A1 and ROS overexpression are involved in hepatotoxicity of decabromodiphenyl ether (BDE-209), Toxicol. Lett. 352 (2021) 26, https://doi.org/10.1016/j.toxlet.2021.09.008.
[42] H.L. Claahsen-van der Grinten, P.W. Speiser, S.F. Ahmed, et al., Congenital adrenal hyperplasia-current insights in pathophysiology, diagnostics, and management, Endocr. Rev. 43 (1) (2022) 91, https://doi.org/10.1210/endrev/bnab016.
[43] J. Zhai, V.H. Man, B. Ji, et al., Comparison and summary of in silico prediction tools for CYP450-mediated drug metabolism, Drug Discov. Today 28 (10) (2023) 103728, https://doi.org/10.1016/j.drudis.2023.103728.
[44] S. Lin, J. Wei, B. Yang, et al., Bioremediation of organic pollutants by white rot fungal cytochrome P450: the role and mechanism of CYP450 in biodegradation, Chemosphere 301 (2022) 134776, https://doi.org/10.1016/j.chemosphere.2022.134776.
[45] R. Zhang, P. Li, X. Shi, et al., Insights into the metabolic mechanism of PBDEs catalyzed by cytochrome P450 enzyme 3A4: a QM/MM study, Chemosphere 278 (2021) 130430, https://doi.org/10.1016/j.chemosphere.2021.130430.
[46] D.M. Butryn, L.H. Chi, M.S. Gross, et al., Retention of polybrominated diphenyl ethers and hydroxylated metabolites in paired human serum and milk in relation to CYP2B6 genotype, J. Hazard Mater. 386 (2020) 121904, https://doi.org/10.1016/j.jhazmat.2019.121904.
[47] Y. Song, R.M. Slominski, S. Qayyum, et al., Molecular and structural basis of interactions of vitamin D3 hydroxyderivatives with aryl hydrocarbon receptor (AhR): an integrated experimental and computational study, Int. J. Biol. Macromol. 209 (Pt A) (2022) 1111, https://doi.org/10.1016/j.ijbiomac.2022.04.048.
[48] N.A. Eti, S. Flor, K. Iqbal, et al., PCB126 induced toxic actions on liver energy metabolism is mediated by AhR in rats, Toxicology 466 (2022) 153054, https://doi.org/10.1016/j.tox.2021.153054.
[49] E.F. de Araújo, F.V. Loures, N.W. Preite, et al., AhR ligands modulate the differentiation of innate lymphoid cells and T helper cell subsets that control the severity of a pulmonary fungal infection, Front. Immunol. 12 (2021) 630938, https://doi.org/10.3389/fimmu.2021.630938.
[50] C. Gutiérrez-Vázquez, F.J. Quintana, Regulation of the immune response by the aryl hydrocarbon receptor, Immunity 48 (1) (2018) 19, https://doi.org/10.1016/j.immuni.2017.12.012.
[51] B.A. Creamer, S.N.B. Sloan, J.F. Dennis, et al., Associations between pregnane X receptor and breast cancer growth and progression, Cells 9 (10) (2020), https://doi.org/10.3390/cells9102295.
[52] Y. Fu, Z. Bi, H. Ji, et al., Disruption of the tumor suppressor-like activity of aryl hydrocarbon receptor by arsenic in epithelial cells and human lung cancer, Int. J. Biol. Sci. 19 (7) (2023), https://doi.org/10.7150/ijbs.81423, 1983.
[53] W. Zhang, Z. Wang, Y. Fu, et al., Aryl Hydrocarbon Receptor (AHR) suppresses arsenic (As(3+))-Induced malignant transformation by antagonizing TOX expression, Int. J. Biol. Sci. 21 (6) (2025) 2747, https://doi.org/10.7150/ijbs.107268.
[54] G. Vázquez-Gómez, J. Petráš, Z. Dvořák, et al., Aryl hydrocarbon receptor (AhR) and pregnane X receptor (PXR) play both distinct and common roles in the regulation of colon homeostasis and intestinal carcinogenesis, Biochem. Pharmacol. 216 (2023) 115797, https://doi.org/10.1016/j.bcp.2023.115797.
[55] D.P. Hill, P. D'Eustachio, T.Z. Berardini, et al., Modeling biochemical pathways in the gene ontology, Database : the journal of biological databases and curation (2016), https://doi.org/10.1093/database/baw126, 2016.
[56] A.M. Richard, R.S. Judson, K.A. Houck, et al., ToxCast chemical landscape: paving the road to 21st century toxicology, Chem. Res. Toxicol. 29 (8) (2016) 1225, https://doi.org/10.1021/acs.chemrestox.6b00135.
[57] AOPXplorer. http://apps.cytoscape.org/apps/aopxplorer. (Accessed 21 February 2019).